PCCP

ROYAL SOCIETY OF CHEMISTRY

PAPER

View Article Online
View Journal | View Issue

Cite this: *Phys. Chem. Chem. Phys.*, 2024, **26**, 13106

Extreme ultraviolet time-resolved photoelectron spectroscopy of adenine, adenosine and adenosine monophosphate in a liquid flat jet†

Masafumi Koga, [a] Do Hyung Kang, [a] Zachary N. Heim, [a] Philipp Meyer, [b] Blake A. Erickson, [a] Neal Haldar,[a] Negar Baradaran,[a] Martina Havenith [b] and Daniel M. Neumark *[ac]

Received 28th February 2024,
Accepted 10th April 2024

DOI: 10.1039/d4cp00856a

rsc.li/pccp

Time-resolved photoelectron spectroscopy using an extreme-ultraviolet (XUV) probe pulse was used to investigate the UV photoinduced dynamics of adenine (Ade), adenosine (Ado), and adenosine-5-monophosphate (AMP) in a liquid water jet. In contrast to previous studies using UV probe pulses, the XUV pulse at 21.7 eV can photoionize all excited states of a molecule, allowing for full relaxation pathways to be addressed after excitation at 4.66 eV. This work was carried out using a gas-dynamic flat liquid jet, resulting in considerably enhanced signal compared to a cylindrical jet. All three species decay on multiple time scales that are assigned based on their decay associated spectra; the fastest decay of ~100 fs is assigned to ππ* decay to the ground state, while a smaller component with a lifetime of ~500 fs is attributed to the nπ* state. An additional slower channel in Ade is assigned to the 7H Ade conformer, as seen previously. This work demonstrates the capability of XUV-TRPES to disentangle non-adiabatic dynamics in an aqueous solution in a state-specific manner and represents the first identification of the nπ* state in the relaxation dynamics of adenine and its derivatives.

1 Introduction

The photophysics and photochemistry of nucleic acid constituents (NACs) are of fundamental interest from the perspective of understanding biological damage induced by ultraviolet light.[1–3] Despite the large cross sections of NACs in the ultraviolet (UV) regime, DNA is known to be remarkably photostable, as evidenced by the quantum yields of photodamage being less than 1%.[4,5] Research has focused on elucidating the underlying mechanisms of photostability, *i.e.* how the excess energy is efficiently dissipated in a non-destructive manner before inducing bond cleavage that can lead to biological damage.[6–11] A better understanding of the processes at the molecular level is crucial not only for a bottom-up understanding of the biological effects of UV light, but for elucidating the reasons for the selection of nucleobases as the elements of building blocks that define the genetic code.[12,13] To this end, we have applied extreme ultraviolet time-resolved photoelectron spectroscopy (XUV-TRPES) to investigate the relaxation dynamics of aqueous adenine (Ade), its nucleoside adenosine (Ado), and nucleotide adenosine-5-monophosphate (AMP), the structures of which, including two tautomeric forms of Ade, are shown in Scheme 1.

The absorption spectra of Ade, Ado and AMP are nearly identical.[4] The lowest absorption band centered at ~260 nm consists of overlapping bands of ππ* excitations localized on the adenine moiety, L_a (HOMO → LUMO) and L_b (HOMO−2 → LUMO and HOMO → LUMO+1). Theoretical studies indicate that the L_a state carries the majority of the oscillator strength, while the close lying nπ* state is optically dark.[3] For Ade in the gas phase, the most commonly accepted relaxation mechanism is the stepwise S_2 (ππ*) → S_1 (nπ*) → S_0 (gr) pathway based on biexponential decay with ultrafast (<100 fs) and slower (0.75–1.1 ps) time constants.[14–19] This mechanism is supported by numerous theoretical studies showing there are two conical intersections (CIs) of the excited states coupled with the ground state characterized by puckering of the pyrimidine ring at the C2 atom for the S_0/L_a CI (^{2}E) and puckering at the C6 atom for the $S_0/n\pi^*$ CI ($^6S_1$).[3,20–28]

The effect of the aqueous environment on the relaxation dynamics, on the other hand, still remains elusive in many respects. Many femtosecond time-resolved experiments have been performed for aqueous NACs containing the adenine moiety, including transient absorption (TA),[2,29–32] Kerr-gated time-resolved fluorescence (KTRF),[31] fluorescence upconversion (FU),[33–39] and TRPES.[40,41]

[a] *Department of Chemistry, University of California, Berkeley, California 94720, USA. E-mail: dneumark@berkeley.edu*
[b] *Lehrstuhl für Physikalische Chemie II, Ruhr-Universität Bochum, 44801, Germany*
[c] *Chemical Sciences Division, Lawrence Berkeley National Laboratory, Berkeley, California 94720, USA*

† Electronic supplementary information (ESI) available. See DOI: https://doi.org/10.1039/d4cp00856a

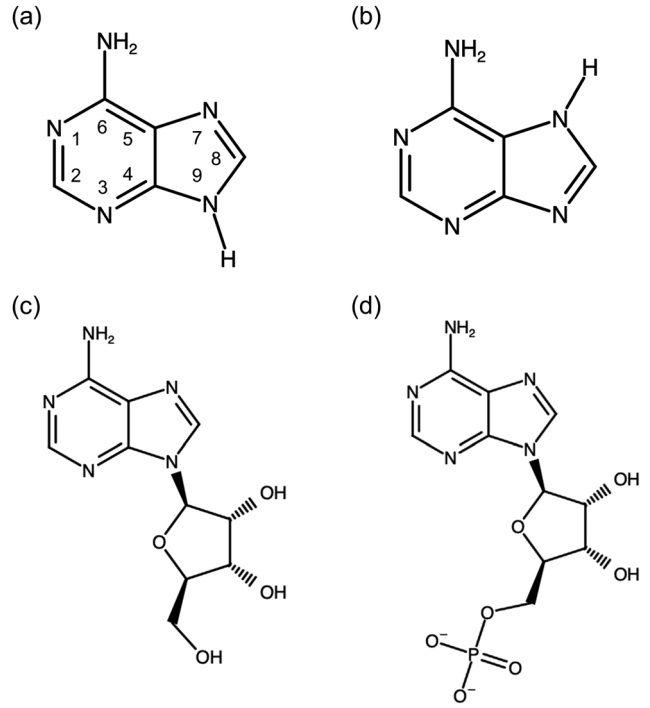

Scheme 1 Molecular structures of (a) 9H-Ade, (b) 7H-Ade, (c) Ado, and (d) AMP.

Theoretical work has considered the effect of solvation on the excited state dynamics[37,42–49] Although there is experimental and theoretical consensus that excited state relaxation of Ado, AMP, and 9H Ade, is complete within 1 ps, there has been disagreement on whether the initially excited ππ* state relaxes directly to the ground state or if the nπ* state plays a role. The differences with respect to the accepted gas phase mechanism arise because in solution, the nπ* state is destabilized relative to the ππ* state, so its vertical excitation energy is higher than that of the ππ* state.[3,43,47–49] Relaxation is characterized by single or multiple timescales, depending on the experiment, which raises the question of which electronic states are involved. While some NAMD studies predicted the involvement of the nπ* state in relaxation,[44,45] others suggested from the calculations of the vertical excitation energies that the nπ* is highly destabilized in water and thus excluded from the ultrafast relaxation.[47–49] Moreover, two tautomeric forms, the canonical 9H form and the 7H form, are approximately equivalent in energy in aqueous solution, so both are expected to contribute to dynamics by the UV excitation.[50,51] The excited state lifetimes for 9H- and 7H-tautomers have been determined at 0.1–0.6 ps and ∼9 ps, respectively.[30,32,35,36,40] Based on the similarity in the obtained time constants and the structural correspondence, the dynamics of canonical 9H adenine are considered to be similar to those of Ado and AMP.[2,30,34,35,40]

These considerations motivated studies of electronic relaxation in adenine and its derivatives using liquid jet TRPES, since such an experiment can in principle detect both ππ* and nπ* states *via* one-photon ionization. Experiments using UV pump and probe pulses were carried in by Lübcke[40] and, later, in our laboratory.[41] In the first study, in which aqueous Ade and Ado were excited at 4.66 eV and ionized at 5.0–5.2 eV, a monoexponential decay with a time constant of 100–215 fs depending on the ionization photon energy was obtained for Ado. For Ade, two time constants in its biexponential decay of 60–80 fs and 2–8 ps were attributed to the deexcitation of the 9H- and 7H-tautomers, respectively. The liquid jet TRPES study in our group with a probe photon energy of 6.2 eV interrogated the relaxation dynamics of Ado and AMP following the ππ* excitation at 4.69–4.97 eV, where a lifetime of ∼210–250 fs was extracted in both systems. However, UV/UV TRPES experiments can give misleading results if the probe photon energy is too low (in both gas phase and solution) since the evolving system can drop out of the "ionization window" determined by the probe photon energy.[52,53] Also, the difficulty of preparing an ultrashort UV pulse can limit the time resolution of the experimental apparatus: the instrumental response function (IRF) was ∼170 fs in the experiment with the 6.2-eV probe.

To address the limitation of TRPES using a UV probe, several groups have incorporated femtosecond XUV probe energies at photon energies above 20 eV into their experiments. Liquid jet XUV-TRPES experiments have been reported by Suzuki,[54–57] Kornilov,[58] Chergui,[59,60] and Wörner.[61,62] These experiments present their own set of challenges. The probe energy is sufficient to ionize the water in addition to the much more dilute solute, so one has to take care that the weak solute pump–probe signal is not overwhelmed by water photoelectrons. In addition, unless the UV pump pulse is very weak, there are time-dependent space charge effects induced by UV ionization of the solute that can distort the TRPE spectra, particularly at long delay times.[63] Nonetheless, Suzuki has recently had considerable success with liquid jet XUV-TRPES and has reported a systematic study of photoexcited pyrimidine bases.[54]

Here, we carry out XUV liquid jet TRPES on Ade, Ado, and AMP using a 4.7 eV pump pulse and 22 eV probe pulse formed by high harmonic generation. A key advance in this work is the replacement of the 30 μm diameter cylindrical liquid jet used in our previous work (and in most liquid jet photoelectron spectroscopy experiments) with a flat liquid jet run in the "gas dynamic" mode,[64] resulting in much better spatial overlap with the incident UV and XUV light pulses and suppressed ionization of the water vapor jacket that surrounds a liquid jet; details of flat jet operation are discussed in the following section.

We find that all three systems undergo decay on two timescales, 100 fs and 500 fs. Global lifetime analysis yields decay-associated spectra that indicate the faster timescale, which accounts for most of the time-dependent signal, is associated with the initially excited ππ* state and the slower with the nπ* state. To our knowledge, these results represent the first spectroscopic observation of the nπ* state. In addition, we observe a long-lived signal for Ade attributed to the 7H tautomer, consistent with the interpretation of earlier UV/UV TRPES.[40]

2 Experimental

The experiment comprises a vacuum chamber housing the liquid jet and photoelectron spectrometer, and a beamline

where the femtosecond UV and XUV pulses are generated. The vacuum chamber, described in detail previously,[65,66] has two differentially pumped regions: the liquid jet region, where a flat jet is formed and collected in a liquid-N_2 cooled trap, and a magnetic bottle photoelectron spectrometer.[67] The flat jet and XUV capabilities of the instrument are new and are described in more detail below.

2a Sample

Adenine (Ade, Sigma-Aldrich, 5 mM), adenosine (Ado, 7 mM), adenosine-5′-monophosphate (AMP, 10 mM) solutions are prepared with a buffer solution at pH = 7.18 with 40 mM of Trizma HCl and 15 mM of NaOH to partially neutralize it to form buffer conditions. 25 mM NaCl is further added to suppress streaming currents and associated jet charging.[68–70] Trizma has been reported to be an effective corrosion inhibitor of steel,[71] allowing reuse of samples after collection in the LN_2-cooled trap, in principle. An HPLC pump (Shimadzu, LC-40i) delivers the sample solutions to the microfluidic chip from which the flat jet is formed.

2b Liquid flat jet

Fig. 1a shows a photograph of a flat jet in operation under typical experimental conditions; the jet is formed using a microfluidic chip device from Micronit BV shown in the inset.[64] The chip consists of three channels: a 30 μm central channel and two outer 50 μm channels that merge with the central channel at 40° at the tip of the jet. This device has been used by our group in molecular beam scattering experiments where a flat jet is formed by flowing liquid through the two outer channels; the central channel is not used.[72,73] The flat jet thus produced in so-called "colliding-jet" geometry has been used in XUV photoelectron spectroscopy by Winter[74] and Suzuki.[75] In our TRPES experiment, we operate the flat jet in the "gas dynamic" mode, in which liquid flows through the central channel and He gas flows through the two outer channels, flattening the liquid jet and producing the image in Fig. 1a. Both the liquid flow rate and gas load on the chamber are reduced in the gas dynamic mode; other advantages are described below.

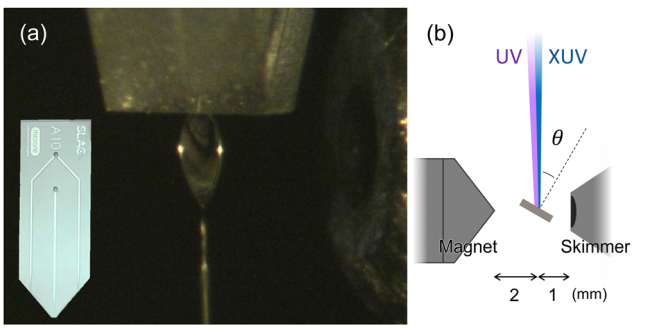

Fig. 1 (a) Photo of gas-dynamic flat jet in operation. Inset shows the flat jet tip (Micronit) used in the experiment. (b) Schematic of the top view of the laser interaction region. The flat jet is ∼1 mm away from skimmer with a 500 μm orifice and a magnetic cone is placed ∼2 mm away from the jet. The UV/XUV angle of incidence with the jet (θ) is set at 30–60° to optimize photoelectron collection efficiency.

In normal operation, the liquid sample delivery rate is 0.2 mL minute^{-1}, controlled by the HPLC pump, and the He input gas pressure is approximately ∼300 kPa (monitored by Wika #111.11.53) to produce a stable flat jet. The flat jet image in Fig. 1a has a dimension of about 200(w) × 500(l) μm and shows a strong interference fringe, demonstrating the ultrathin (<1 μm) nature of the sheet. This sheet size provides better spatial overlap with the pump and probe pulses than a cylindrical jet. The jet is located 1 mm away from a 500 μm skimmer that serves as the entrance orifice to the magnetic bottle photoelectron spectrometer. We found that the photoelectron intensity is maximized and similar for laser/flat jet incident angles ranging from 30–60° (Fig. 1b).

2c Femtosecond laser pulses

A schematic diagram for XUV-TRPES with a 266-nm (4.66-eV) pump is described in Fig. 2. A 7 mJ, 35 fs laser pulse centered at 797 nm is produced by a femtosecond regenerative amplifier system (Astrella, Coherent) operated at a repetition rate of 1 kHz. The pulse is split by a set of beamsplitters. 1 mJ is delivered to a third harmonic generation setup consisting of a pair of β-barium borate (BBO) crystals to generate a UV pump pulse at 266 nm. Another 1 mJ is sent to a TOPAS (Coherent) that can generate tunable visible and UV light but is only used for a calibration of the photoelectron spectrometer. The remaining 5 mJ is frequency-doubled in a 200-μm thick BBO crystal and any unconverted fundamental is removed using a 1-mm thick dichroic mirror. The isolated 400-nm beam (900 μJ) passes through a 1 m focal length plano-convex lens and is focused at the exit of a 60-cm semi-infinite gas cell (SIGC)[76] filled with Kr gas at 3 torr, resulting in XUV light from high harmonic generation (HHG).

HHG results in odd harmonics of the driving laser that are spaced by 6 eV for a 400 nm driver. We wish to obtain spectrally pure light at 22 eV, the 7th harmonic. After the SIGC, the light propagates through a 200-nm thick Al filter that transmits XUV harmonics above 15 eV and blocks residual 400-nm light. The filtered XUV is then guided to a toroidal mirror at an incident angle of 4° that focuses it onto the sample. Right after the toroidal mirror, the beam is turned by 90° by a multilayer mirror designed by the Center for X-Ray Optics at Lawrence Berkeley National Laboratory to selectively reflect the 7th harmonic of the 400 nm driving pulse. Residual 9th harmonic is removed by a 200-nm Sn filter downstream of the multi-layer mirror.

The UV pump beam is coupled into vacuum through a 2-mm CaF_2 window. The XUV and UV beams are combined by means of an annular concave mirror with a focal length of 1 m; the XUV beam passes through the annular hole while the UV beam is reflected and focused onto the sample. This configuration enables pump–probe spatial overlap at a minimal crossing angle, approximately 0.5°. Using a curved mirror for focus instead of a convex lens also preserves temporal characteristics of the pump pulse. The IRF of the setup is evaluated by measuring the intensity of UV sidebands in the XUV photoelectron spectra of Ar, Xe, and the liquid water jet using the laser-

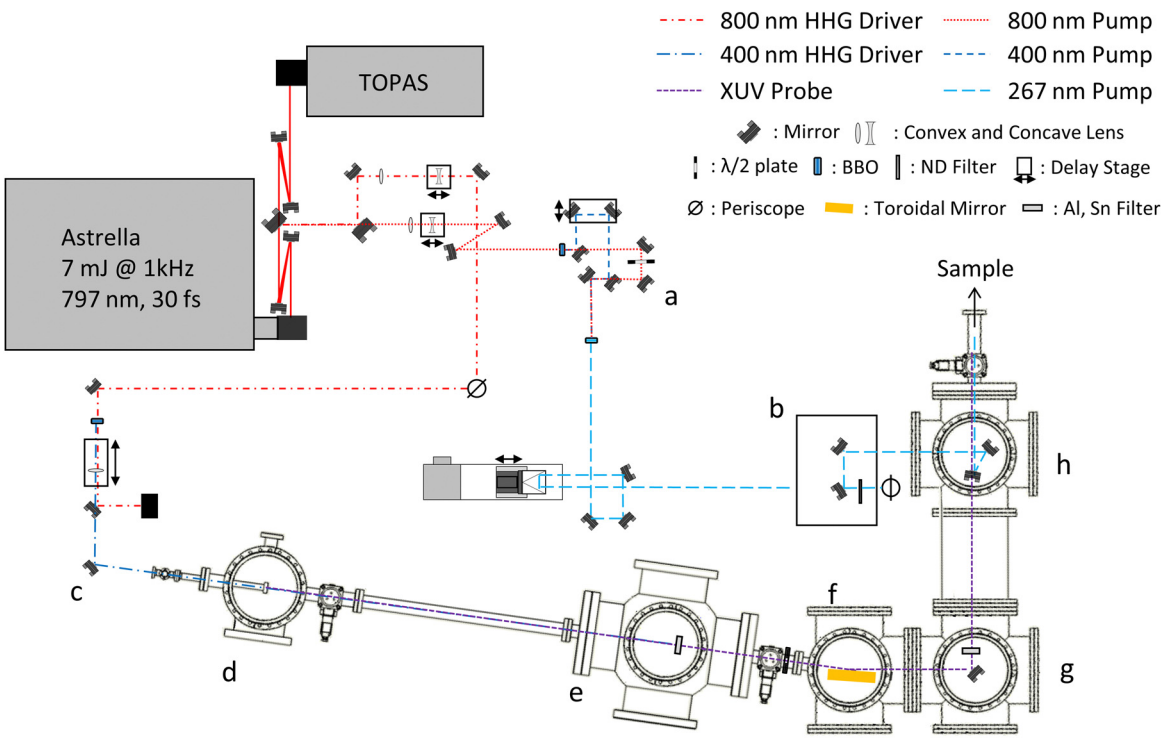

Fig. 2 Optical setup for 266-nm pump/XUV (21.7 eV) probe experiment. Layout consists of (a) BBO-based third harmonic generation setup, (b) breadboard above table for coupling into vacuum, (c) second harmonic generation setup for HHG, (d) semi-infinite gas cell (SIGC), (e) 200-nm thick Al filter, (f) toroidal mirror, (g) multilayer mirror, and (h) annular mirror where the pump pulse is combined.

assisted photoelectric effect (LAPE)[59,77–79] and is found to be 30 fs (1σ). A result of LAPE measurement of H_2O flat jet (NaCl 25 mM) is shown in Fig. S1 (ESI†). The spatial cross-correlation of pump and probe pulses is estimated at 150 μm by tracking the Ar LAPE intensity while scanning the UV pump pulse vertically and horizontally, where the step sizes of the piezoelectric motors on the mirror controlling the pointing are calibrated by imaging the beam spot with a CMOS camera sensor (Imaging Source, DFK72BUC02). In all experiments, the UV pulse energy is at *ca.* 250 nJ at the sample position, while the XUV probe pulse energy is 2–5 nJ.

2d Photoelectron detection

Photoelectrons are directed by the inhomogeneous magnetic field of the magnetic bottle time-of-flight (ToF) photoelectron spectrometer comprising a stack of neodymium magnets with a soft iron cone and a solenoid maintaining 8G homogeneous field in a 66-cm ToF tube. Photoelectrons are detected by chevron-stack microchannel plates (MCPs) coupled to a phosphor screen; the screen is used only for the alignment of the magnetic bottle. Signal pulses from the anode are amplified by a variable gain preamplifier (Stanford Research Systems, SR446) before being transmitted to an ADC digitizer card (Acqiris, U5309A).

The observed photoelectron kinetic energy (eKE) is calibrated using Ar, for which the ionization energy of 15.76 eV,[80] and Xe with ionization energies of 12.13 eV for Xe^+ ($^2P_{3/2}$) and 13.44 eV for Xe^+ ($^2P_{1/2}$).[81] LAPE measurements of Ar are also employed with the 266-nm pump pulse, yielding more data points from the XUV + UV sidebands and thus improving the accuracy of the calibration procedure.

Photoelectron spectra for each time delay are acquired for over 10^6 shots for Ado, 600 000 shots for AMP, and 650 000 shots for Ade. Because photoelectrons from the liquid- and gas-phase water are obtained simultaneously in addition to the solute pump–probe signals, the light-induced shift of the liquid peak relative to the static gas peak position is monitored in the experiment (see Section 3b for more details).

3 Results

3a Flat *vs.* cylindrical liquid jet

Fig. 3 shows one-photon XUV (21.7 eV) photoelectron spectra of Ado aqueous solution (see Section 2) obtained with a 30 μm diameter cylindrical jet running at 1.0 mL min^{-1} through a fused-silica capillary and a flat jet with the microfluidic chip device operating in the gas dynamic mode. Spectra are plotted as a function of electron binding energy (eBE): eBE = $h\nu_{XUV}$ − eKE. The photoelectron spectrum of the cylindrical jet shows two sharp peaks from ionization out of the $1b_1$ (eBE = 12.5 eV) and $3a_1$ (14.7 eV) molecular orbitals of gas phase H_2O in the vapor jacket surrounding the liquid jet; the broad weaker feature at ∼11.3 eV is from the $1b_1$ orbital of liquid water. Similar spectra have been recorded by Winter and others.[58,82,83]

In the flat jet spectrum, the broad liquid features are considerably enhanced relative to the gas phase peaks. This is

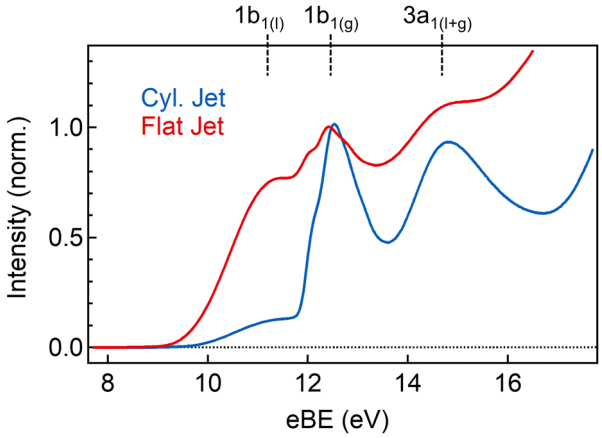

Fig. 3 One photon photoelectron spectra of an aqueous Ado solution depending on the mode of a jet; a 30-μm cylindrical jet (blue) and a flat jet (red).

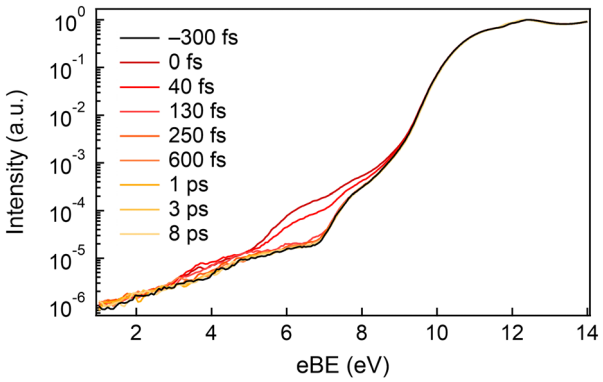

Fig. 4 Spectral lineouts for Ado obtained using UV pump (267 nm, 250 nJ per pulse) and XUV (21.7 eV) probe with the space-charge shift corrected.

partly due to better spatial overlap between the XUV beam and the flat jet. However, a comparison to the X-ray photoelectron spectrum reported by Winter on a flat jet formed by colliding two cylindrical jets shows that there is substantial suppression of the vapor features in our spectrum.[74] We take this to mean that in a gas-dynamic flat jet, the He sweeps away much of the vapor jacket, greatly reducing the gas phase contribution to the photoelectron spectrum. Note that He does not absorb XUV light at 21.7 eV[84] so there is no deleterious effect from the He side jets.

3b Time-dependent signals and the space-charge correction

In the time-resolved measurements, relatively high photoelectron yields from both pump and probe pulses induce time-dependent space charge effects that arise as a kinetic energy shift of the probe photoelectrons from the solution.[55,58,63] As discussed by Kornilov,[58] the most troublesome effect of these results from pump-pulse ionization of solute molecules *via* resonant multiphoton ionization. Photoelectrons produced by this process are ejected into vacuum, leaving a net positive charge on the jet, and this net charge slows photoelectrons generated by the XUV pulse coming after the UV pulse. Moreover, this shift is dependent on the pump–probe delay and is larger for longer delay times. This effect must therefore be corrected in order to carry out an accurate background subtraction. To measure the shift of the liquid water features with delay time, the positions of the $1b_{1(g)}$ and $1b_{1(l)}$ peaks at each time delay are fit to a double-Gaussian, yielding a time-dependent space-charge shift that can be applied to the TRPE spectrum at each delay time. Fig. S2a (ESI†) shows an example of the double-Gaussian fit and time-dependent shift for the Ado solution used in our experiments. Under the conditions of the experiment, the shift is as high as −0.2 eV at a delay of 20 ps, the longest time-delay reported in this work (Fig. S2b, ESI†).

Fig. 4 shows spectral lineouts of space charge corrected TRPE spectra of Ado using 267 nm pump and 21.7 eV probe pulses. The validity of the space charge correction is confirmed by the constant position of the water $1b_{1(l)}$ peak (10–12 eV) over time. The baseline spectrum at −300 fs (black line) shows a shoulder around 7.5 eV on the tail of the liquid water peak. The ionization potential of adenine in water has been determined experimentally to be 7.7 eV[85] and agrees well with the eBE of this feature.

In the time-dependent curves, the strong signal at t = 0 fs from 5–8 eV is from the LAPE sideband by the pump pulse.[59] The pump–probe signal, which is the main feature of interest, is the small but discernible signal above the baseline from 3–7 eV that persists for positive delay times.

3c Pump–probe signals

Fig. 5a displays a contour plot of the baseline subtracted TRPE spectra of Ado out to 2 ps. Those of AMP and Ade are available in Fig. S3 and S4 (ESI†). A positive signal is observed out to 3 eV eBE, along with an intense LAPE signal above 5 eV at the time origin. Fig. 5b shows an expanded view of the lowest eBE signal at short delay times. To extract the signal from the excited state of NACs, the LAPE feature is subtracted from the plot using the procedure described in Section 4. The results are presented in Fig. 5c for Ado, 5d for AMP, and 5e and f for Ade, respectively. Note that the contour plot for the NaCl H_2O result (Fig. S1, ESI†) reproduces the same feature at t = 0. However, we do not use this result without chromophores to subtract from the pump–probe data because the background photoelectron spectrum depends significantly on jet conditions that are highly susceptible to the choice of solutes. Thus we subtract the LAPE contribution by global lifetime analysis, as explained in detail in Section 4.

In Fig. 5b, the spectrum predominantly comprises two features: one <4.2 eV and the other from 4.2–4.7 eV. The lower eBE peak appears to shift from 3.7 to 4.0 eV within 50 fs and the 4.0-eV feature starts to decay around 100 fs. There is a similar trend of shift in the higher eBE feature (4.2–4.8 eV) although it is less prominent because of the overlap with the first peak. These short-time effects, while subtle, are real and are not affected by, for example, space charge effects that are very small at short time delays (Fig. S2b, ESI†).

LAPE subtraction in Fig. 5c reveals strong signals at binding energies greater than 6 eV that appear immediately after

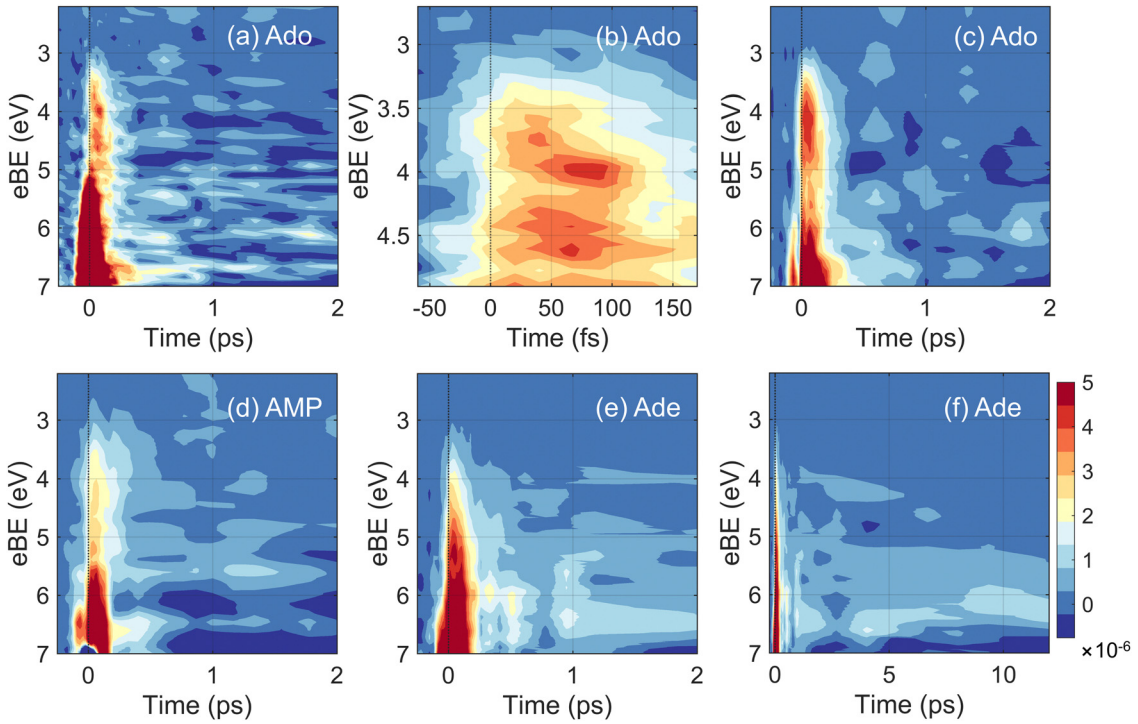

Fig. 5 Contour plots of the baseline-subtracted pump–probe signals. (a) Ado without smoothing. (b) Expanded view of (a) around t = 0. (c)–(f) LAPE-subtracted TRPE spectra of (c) Ado, (d) AMP, (e) and (f) Ade at short and long time delays, respectively. 9-Point spectral smoothing is applied to all LAPE-subtracted plots in c–f and 3-point temporal smoothing is additionally applied to the AMP data (d).

photoexcitation along with the feature at 3–5 eV. Much of the signal across the spectrum disappears by 200 fs, but signal above 5 eV persists out to 1 ps. The overall appearance of the spectrum is consistent with excited states of Ado relaxing to the ground state on an ultrafast (<1 ps) timescale. The AMP signal (Fig. 5d) is weaker but exhibits similar time evolution similar to Ado.

Fig. 5e and f show LAPE-subtracted TRPE spectra of Ade at time delays out to 2 and 12 ps, respectively. In contrast Ado and AMP, Ade signal from 5–7 eV persists out to 12 ps. In contrast to Ado and AMP, the intense feature of Ade does not completely decay in an ultrafast timescale. A significant portion of the signal at 4 eV remains over 5 ps, while a feature in the higher eBE region is seen throughout our detection time window.

4 Analysis

To obtain an overall view of the relaxation dynamics, the background-subtracted TRPE spectra of Ado (Fig. 5a), AMP (Fig. S3, ESI†), and Ade (Fig. S4, ESI†) are further analyzed using Global Lifetime Analysis (GLA). In this analysis, the overall 2D dataset $S(\mathrm{eBE}, t)$ is expressed as a sum of exponential functions convolved with an instrumental response function $L(t)$:

$$S(\mathrm{eBE}, t) = \left[S_0(\mathrm{eBE}) + \sum_{i=1}^{n} \mathrm{DAS}_{\tau_i}(\mathrm{eBE}) \cdot \exp(-t/\tau_i) + c \right] \times L(t) \quad (1)$$

where

$$L(t) = \frac{1}{\sigma\sqrt{2\pi}} \exp\left(-\frac{t^2}{2\sigma^2}\right) \quad (2)$$

In eqn (1), n is the number of time constants required for a fit. The coefficients of each exponential component are referred to as the Decay Associated Spectrum: $\mathrm{DAS}_{\tau_i}(\mathrm{eBE})$. The parameter c is the residual constant signal that represents either background noise or a very long-lived state. The prefactor $S_0(\mathrm{eBE})$ represents the coherent spike due to the LAPE sideband at t = 0. Subtraction of its time profile $S_0(\mathrm{eBE})\cdot L(t)$ from the dataset gives the intrinsic time evolution for the photoexcited chromophores. The analyses are performed from −300 fs to 6 ps for Ado and AMP, and from −300 fs to 20 ps for Ade. To improve the fitting quality, a 9-point boxcar averaging in energy is applied to all datasets. The data for AMP is further smoothed in time by three points which we confirm does not significantly alter the time profiles (Fig. S5, ESI†). The LAPE-subtracted, smoothed TRPE spectra for the three NACs are shown in Fig. 5c–f.

For all three systems, all or most (for Ade) signal decays within 1 ps, and the number of exponential functions to reproduce each dataset is carefully and mutually considered. In all datasets within 2 ps, two time constants of at *ca.* 100 and 500 fs always give smaller residuals than a single time constant with *ca.* 150 fs, as shown in Fig. S6–S9 (ESI†). The difference between monoexponential and biexponential fits for Ado is subtle. However, after analyzing the datasets for AMP and Ade,

which exhibited significantly smaller residuals for the biexponential fit within 2 ps, we concluded that the biexponential decay better represents the dynamics. Consequently, two time constants are required to adequately fit the data set for Ado and AMP, leaving no long-lived offset above the noise level while three time constants with the positive offset component are needed for Ade to account for the overall decay. The time constants and DASs are shown in Fig. 6 for all three NACs.

The two DASs obtained for Ado are displayed in Fig. 6a. DASτ_1 (110 $\pm$ 10 fs) covers the entire spectral region of Ado with peaks at 4.0 and 4.8 eV and a slope extending towards higher eBE. The second, relatively small, DASτ_2 is obtained with 470 $\pm$ 160 fs and exhibits two peaks at 4.5 eV and 5.3 eV. Analysis using a single exponential decay yields a time constant of 135 fs; in the corresponding DAS shown in Fig. S10 (ESI†) the two peaks seen in the red trace of Fig. 6a are no longer distinct. The obtained fitting curves deviate from the data for eBE $<$4 eV and $>$6 eV (see Fig. S6c and d, ESI†, respectively). DASs in AMP are obtained with similar time constants (τ_1 = 122 $\pm$ 5 fs, τ_2 = 550 $\pm$ 50 fs) and those spectral shapes are roughly similar; DASτ_1 has two peaks at 4.0 and 4.8 eV with a strong feature over 5 eV and DASτ_2 includes peaks at 4.5 eV and 5.3 eV with another peak at 3.7 eV.

In Ade, three time constants (τ_1 = 90 $\pm$ 4 fs, τ_2 = 480 $\pm$ 90 fs, τ_3 = 9.0 $\pm$ 4.9 ps) are required to fit the result out to 20 ps. τ_1 is slightly shorter than for Ado and AMP while τ_2 is the same within error bars. The third, slow component is only seen in Ade. DASτ_1 in the lower eBE region is similar to Ado and AMP, with a peak at 4.0 eV, while the shape and intensity higher than 4 eV can be distinguished with a peak at around 5.4 eV. DASτ_2 comprises two peaks at 4.8 eV and 5.8 eV. DASτ_3 has two peaks at 4.0 eV and 5.0 eV that correspond well with those in DASτ_1 of Ado and AMP. The long-lived offset ($>$20 ps) component has a positive onset around 6 eV that was not seen for Ado or AMP.

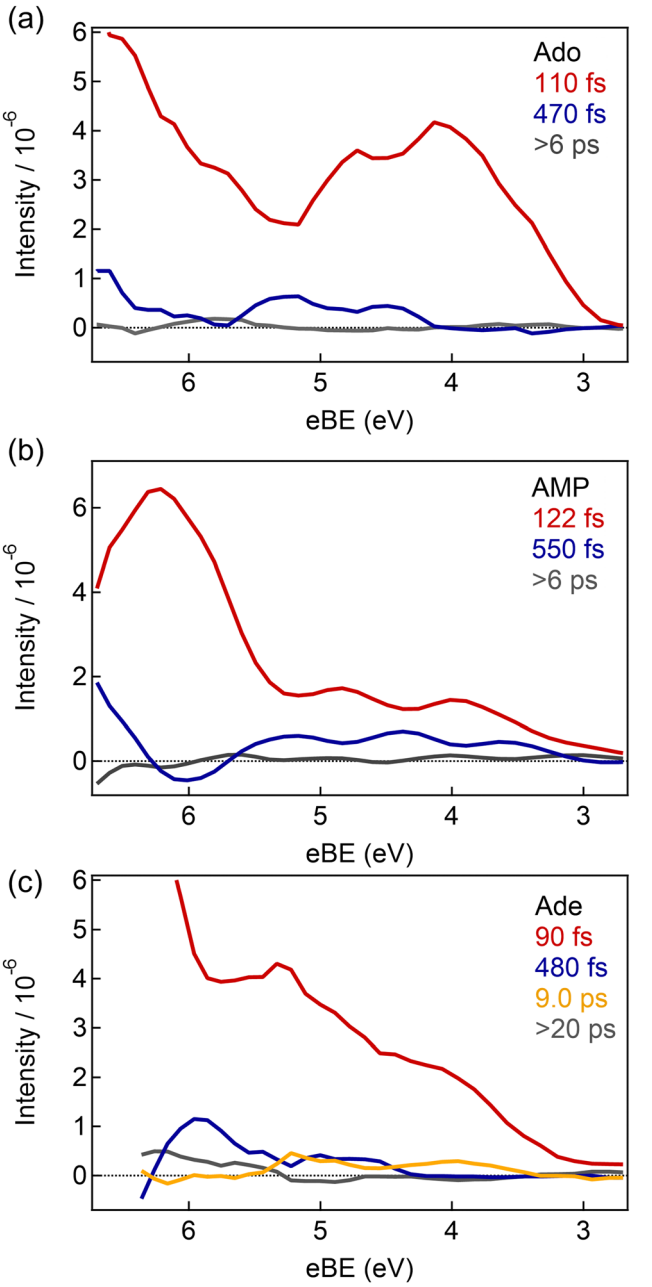

Fig. 6 DASs obtained from GLA for (a) Ado, (b) AMP, and (c) Ade. τ_i for each DAS$_i$ is shown in the same color on the top right. The gray spectra represent the long-lived offset (*c*).

5 Discussion

5a Ado, AMP, and the short time dynamics of Ade

In this study, the relaxation dynamics of adenine and its derivatives in aqueous solution are interrogated by XUV-TRPES, exploiting a high probe energy to access the complete manifold of states throughout the entire relaxation process with high temporal resolution (30 fs). These advantages allow us to assess the non-adiabatic dynamics taking place on an ultrafast timescale.[86] Two time constants, $\sim$100 and $\sim$500 fs, are needed to reproduce the overall evolution in Ado, AMP, and Ade within $<$2 ps. For Ade, we also observe a longer-lived signal that persists for $\sim$9 ps. A similar long-lived signal for Ade was seen in the UV/UV liquid jet TRPE spectrum by Lübcke and co-workers[40] and was attributed to the 7H conformer of Ade, which is expected to comprise 22% of the Ade in solution at 20 °C.[50,51]

It is instructive to compare the results here with our earlier UV/UV TRPES study of Ado and AMP using a 6.2 eV probe photon.[41] In that work, the effective eBE cutoff was about 5.5 eV, owing to poor transmission of the magnetic bottle spectrometer for electron kinetic energies below 0.7 eV. Hence, in Ado, only the lower energy feature starting around 5 eV was fully characterized, and the longer-lived signal at higher eBE was largely missed. The UV/UV data on Ado could be fit by a single exponential decay of 210 fs; the biexponential result from the XUV results reported here reflects the more complete view of the dynamics obtained at the higher probe energy and, to some extent, the improved temporal resolution of the XUV experiment.

5b Assignment of the dynamics

We next consider assignment of the states associated with the two decay constants, focusing on Ado since the signals are

somewhat stronger than for Ade and AMP. The initially populated excited state is safely attributable to the L_a state since it carries most of the oscillator strength.[48] In DASτ_1 for Ado in Fig. 6, the lowest eBE peak at 4.0 eV thus corresponds to the ionization from the π^* orbital, leaving a hole on the HOMO π orbital (D_0) and the second peak at $\sim$4.8 eV is likely due to the ionization to the second lowest π-hole cationic state. This splitting is consistent with previous studies of photoionization from the ground state of adenine.[53,87,88] The rising signal for eBE $>$5 eV in DASτ_1 is attributed to photoionization to higher excited states of the Ado cation.

DASτ_2 for Ado appears to correspond to ionization from a different electronic state. It includes two peaks at 4.5 and 5.3 eV, both of which are 0.5 eV higher than the two peaks in DASτ_1. From a theoretical study of the gas-phase photoelectron spectrum of adenine, the lowest n-hole cation is the D_1 state, which is located at 0.65–1.0 eV above D_0, while the second lowest n-hole cation, D_3, is 0.4–0.7 eV above the D_2 level.[53] Based on Koopmans' theorem, ionization from the $\pi\pi^*$ excited state to the n-hole cation is forbidden, as is ionization from the $n\pi^*$ state to a π-hole cation. Thus, one can reasonably relate the alternating peak positions of DASτ_1 and DASτ_2 to the progression of the D_{0-3} ionization series with different hole characters, suggesting that DASτ_2 corresponds to ionization out of the $n\pi^*$ state, and that this state is responsible for the slower decay of $\sim$500 fs. This interpretation is consistent with gas-phase TRPES where the peaks of the first and second DASs are separated by 1 eV and have binding energies reasonably corresponding to D_0 and D_1.[15] The smaller energy difference between the first peaks of DASτ_1 and DASτ_2 in the current study is attributed to the strong destabilization of the $n\pi^*$ state in water.[3] The second time constant with $\sim$500 fs is found in AMP and Ade as well, suggesting that the $n\pi^*$ state participates in the dynamics independently of the sugar and phosphate group.

Another possibility for the longer decay component is relaxation of vibrationally hot ground state molecules formed from by passage through the $L_a \rightarrow S_0$ CI. Based on previous UV-VIS TA and TR-IR studies,[30,32,89–92] repopulation of the thermalized ground state recovery is complete within $\sim$2 ps of photoexcitation for all three NACs. Pecourt *et al.*[29] calculated the initial vibrational temperature in the ground state to be $\sim$1200 K assuming that all the electronic energy released by internal conversion to the ground state is converted to vibrational energy that undergoes intramolecular vibrational redistribution before any cooling by the solvent. Even under this assumption, which serves as an upper bound for the ground state vibrational temperature, most vibrational modes of the Ado are not FC active and we would not expect a broadening of the ground state band by more than 1 eV.[93–95] Therefore, if this contribution were present, it would be expected to appear around 6–7 eV, but it is unlikely to account for the 500 fs decay observed here at considerably lower eBE.

Finally, we consider the earliest dynamics shown in Fig. 5b, where peak shifts within 100 fs are displayed. These rapid variations in the TRPE spectra are most likely from wavepacket dynamics near the FC region on the initially excited L_a state. We attribute these early dynamics to wavepacket propagation on the repulsive potential accessed by photoexcitation, while the decay of these signals at $\sim$100 fs is from L_a depopulation.

From this analysis and the GLA results, we conclude that the overall relaxation dynamics of Ado, AMP, and 9H-Ade are similar. It is expected that a transition to the $n\pi^*$ state occurs near the FC region. This transition may contribute to the dynamics in Fig. 5b but no quantitative signature for this process can be extracted.

5c Comparison to previous results

The main result of this work is that the sub-ps dynamics of Ade, Ado, and AMP are better fit by a biexponential decay with time constants of around 100 and 500 fs than by a single time constant, and that the slower decay is associated with the $n\pi^*$ state. It is useful to compare our results with previous experiments, summarized in Table S1 (ESI†). While some of these experiments report only a single time constant, typically 200–300 fs, several TA and time-resolved fluorescence experiments report biexponential decay with time constants similar to those found here.[31,34,35] Hence, the observation of biexponential sub-ps decay appears to be reasonable, raising the question of which electronic states are involved in the overall dynamics.

Kwok *et al.*[31] attributed their measured time constants of 130 and 450 fs time to decay of the L_a and L_b states, respectively. Gustavsson *et al.*[37] also observed multiple timescales depending on the fluorescence wavelength and proposed a different mechanism in which the faster time constant is assigned to rapid wavepacket motion in the steep FC region of the L_a state and the slower to $L_a \rightarrow S_0$ internal conversion, with the $n\pi^*$ state playing no role in the dynamics. This interpretation was based on LR-PCM/PBE0 calculations on 9H-Ade-4H_2O, which predict a decreased fluorescence oscillator strength as the nucleobase geometry in the L_a state evolves from planer to the non-planer C2-puckered geometry. In our XUV-TRPES experiment, the DAS for the slow time constant points to ionization out of the $n\pi^*$ state, providing yet another interpretation of the biexponential dynamics, one based on an assigned spectral fingerprint of the $n\pi^*$ state. Furthermore, we believe the rapid wavepacket motion on the L_a state proposed by Gustavsson *et al.*[37] is observed here in Fig. 5a, where the early-time wavepacket dynamics can be distinguished from the subsequent $\sim$100 fs decay attributed to L_a deexcitation.

One then has to consider whether this interpretation is reasonable in the light of previous theoretical and experimental work on adenine and its derivatives. From an experimental perspective, one might argue that since the $n\pi^*$ state is nominally optically dark, it should not contribute to the signals in FU experiments. However, our proposed identification of the $n\pi^*$ state does not contradict previous experimental results. There are several experimental and theoretical indications that this state is mixed with the bright $\pi\pi^*$ state. In the gas phase, resonant two photon ionization and laser induced fluorescence detected strong peaks below the 0–0 band of the $\pi\pi^*$ state.[96–98] The calculation by Broo[99] suggested that out-of-plane distortion in 9H-Ade not only couples the $\pi\pi^*$ to the $n\pi^*$ state, but also

leads to increased FC factors for internal conversion to the ground state, which supports the nπ* state contrubting to the ultrafast decay of this molecule. In solution, Cohen[30] and Pancur[36] proposed that the N7 lone pair taking part in the nπ* state plays a decisive role in the ultrafast decay to account for the sub-10 ps lifetime in 7H-Ade. The contribution of the N7 lone pair in the n hole was confirmed in many theoretical studies.[3,28,48]

From a theoretical perspective, although there is consensus that the vertical excitation energy of the nπ* state is above the ππ* state in solution,[3] the role of this state in the dynamics of photoexcited Ade and its derivatives is unsettled. A semiempirical QM/MM study for aqueous 9H Ade by Thiel and coworkers[45] found strong mixing of the nπ* and ππ* state near the FC region, leading to the $S_2 \rightarrow S_1$ transition within 40 fs. The populated S_1 state acquires a predominant nπ* character, returning to the ground state mainly through the $^6S_1$ CI within 430 fs, while a small contribution from the ^2E (L_a/S_0) CI pathway also occurs. Mitrić suggested a similar, stepwise decay mechanism in the TD-DFTB surface-hopping simulations for microsolvated adenine.[44] A CASSCF study of aqueous 9H Ade instead suggested partial involvement of the L_b state in relaxation through vibronic coupling with the L_a state that had a very small energy difference (<0.2 eV).[43] This mechanism, however, cannot explain the large gap between the peaks of the first and second DAS in our experiment. This study also reports that the nπ*state is lower than the ππ* state in the nonplanar geometry and is, in principle, accessible from the L_a state through a relatively small activation barrier of 0.15 eV, although they exclude this process because the amplitude of the wavepacket propagating at this direction is considered to be small.

Based on our results and the above considerations, we propose schematic potential energy surfaces associated with the relaxation as depicted in Fig. 7. Although the energy of the nπ* state at the FC region is high in aqueous media, it can be populated through a curve crossing from the L_a state at lower energy. The reaction coordinate through the ^2E La/S_0 CI mainly involves C2 puckering while C6 puckering leads to relaxation through ^6S CI (nπ*/S_0). It is unclear what fraction of the excited wavepacket propagates through this relaxation path in lieu of the direct deexcitation through the ^2E CI, and what determines the fate of the wavepacket. Based on the relative DAS intensity, direct relaxation through ^2E CI appears to be the main channel and the detour through the nπ* is minor, assuming that the ionization cross-sections are similar between the two excited states as is the case for pyrimidine nucleobases.[54] Further theoretical treatment with a full solvation model would provide a better understanding of the mechanism in aqueous media.

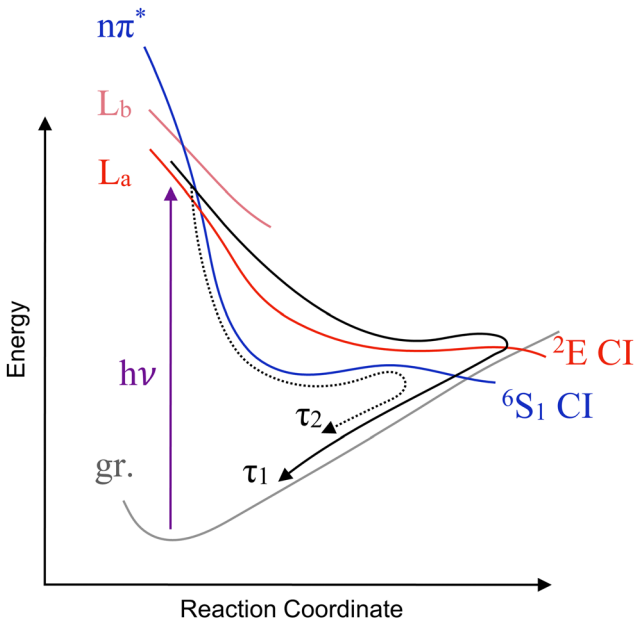

Fig. 7 Schematic potential energy diagram for the three lowest excited states as a function of the reaction coordinate. The direct (L_a to S_0) decay path is represented as the solid arrow and the stepwise path ($L_a \rightarrow$ nπ* $\rightarrow S_0$) as the dotted arrow.

5d Assignment of the excited state dynamics of Ade

As shown in the introduction, Ade forms two tautomers in the ground state: 9H-Ade and 7H- Ade.[50,51] The GLA for Ade yields time constants of 90 fs, 480 fs, and 9 ps. The slowest time constant has been observed in and is consistently attributed to the excited state lifetime of 7H-Ade, while the fast time constants can mainly be associated with 9H-Ade, in line with the other time-resolved experiments such as UV-TRPES,[40] TA,[32] and FU[35,36] on aqueous adenine. This assignment was confirmed by methylation, where 7-methyladenine exhibited only the long excited state lifetime.[30] The only difference we have found here compared to previous works is the presence of the second time scale of 480 fs, attributed to the nπ* state of 9H Ade. This interpretation is consistent with previous work, as discussed above, proposing that the nπ* state associated with the N7 lone pair plays an important role in the ultrafast decay of 9H-Ade, Ado, and AMP.[30,36,99]

The DAS associated with the 9 ps decay can shed some light on the excited state responsible for this decay. Specifically, it exhibits a peak around 4 eV which has been assigned above to ionization to the cationic D_0 state with a π hole, suggesting that the long-lived state of 7H Ade has at least some ππ* character.

Within our experimental timeframe of 20 ps, GLA shows that Ade also exhibits a non-zero offset beyond the 9 ps decay of DASτ_3. This observation, seen for Ade but not Ado or AMP, can be explained by the phosphorescence of 7H-Ade, which is strong in 7-methyladenine but is a few orders of magnitude smaller in Ado.[100] Therefore, the offset band in this study is attributed to the triplet state of 7H-Ade. A DFT/MRCI calculation conducted on isolated 7H Ade predicts a dense manifold of low-lying triplet states in the energy regime between the FC region and the S_1 global minimum.[101] This enables intersystem crossing through multiple El Sayed-rule-allowed pathways of ^{1}ππ*/^{3}nπ* and ^{1}nπ*/^{3}ππ*. Some TA studies associate the long-lived signals with the two-photon ionization of Ade or water.[30,32,90] The current experiment does not find any evidence of the process, as there is no signal in the long time delay around 3.7 eV where the hydrated electron band would be expected.[102]

6 Conclusion

This study investigates the ultrafast UV-induced dynamics of Ade, Ado, and AMP in aqueous solution using XUV-TRPES with a 266 nm (4.66 eV) pump pulse and a 21.7 eV probe pulse. A gas dynamic flat liquid jet is incorporated to form a flat liquid surface approximately 200 μm wide, which provides a larger exposure area to the laser focal spots. This significantly enhances the photoelectron signal from the liquid compared to that obtained by the cylindrical jet. Additionally, the helium gas jet utilized to create the flat jet removes much of the water vapor surrounding the liquid, resulting in the suppression of unwanted gas peak background.

The excited state signals are clearly identified in the 3–7 eV eBE range for all three NACs. Ado and AMP exhibit signals with ultrafast decays that completely merge with the baseline level within 1 ps, whereas long lived signals that can persist over 20 ps are detected in Ade. To reproduce the obtained datasets, GLA is used, which requires two time constants at approximately 100 and 500 fs for Ado and AMP. While the first DAS with distinct peaks at 4.0 and 4.8 eV is safely attributed to the L_a state, the second DAS consists of peaks at $\sim$0.5 eV lower than those of the first DAS, indicating that the $n\pi^*$ state contributes to the relaxation dynamics. Consideration of the early-time (sub- 100 fs) signal suggests that the wavepacket formed by photoexcitation propagates along a steep potential energy surface in the FC region prior to internal conversion. GLA on the Ade spectra yields three time constants, where the first two components at 90 and 480 fs are attributed to 9H-Ade relaxation through a similar mechanisms as Ado and AMP, while the 9-ps component is due to the excited state of 7H-Ade. Overall, this study showcases the ability of XUV-TRPES to disentangle nonadiabatic dynamics in the condensed phase and provide new insights into DNA photophysics on ultrafast timescales.

Conflicts of interest

There are no conflicts of interest to declare.

Acknowledgements

This research is supported by the National Science Foundation Division of Chemistry under Grant No. CHE-2154629 and by CALSOLV, the center for solvation studies at the University of California, Berkeley. M. K. also acknowledges the support from the Japan Society for the Promotion of Science (JSPS) Overseas Research Fellowships. D. H. K. acknowledges Basic Science Research Program through the National Research Foundation of Korea (NRF) funded by the Ministry of Education with Grant No. RS-2023-00241698. P. M. and M. H. acknowledge the support by the Deutsche Forschungsgemeinschaft (DFG, German Research Foundation) under Germany's Excellence Strategy—EXC 2033-390677874—RESOLV. The authors thank W. Yang for his help in implementing the flat jet.

References

1 C. T. Middleton, K. de La Harpe, C. Su, Y. K. Law, C. E. Crespo-Hernández and B. Kohler, *Annu. Rev. Phys. Chem.*, 2009, **60**, 217–239.
2 C. E. Crespo-Hernández, B. Cohen, P. M. Hare and B. Kohler, *Chem. Rev.*, 2004, **104**, 1977–2020.
3 R. Improta, F. Santoro and L. Blancafort, *Chem. Rev.*, 2016, **116**, 3540–3593.
4 D. Voet, W. Gratzer, R. Cox and P. Doty, *Biopolymers*, 1963, **1**, 193–208.
5 M. Shukla and J. Leszczynski, *J. Biomol. Struct. Dyn.*, 2007, **25**, 93–118.
6 J. Cadet, S. Mouret, J. L. Ravanat and T. Douki, *Photochem. Photobiol.*, 2012, **88**, 1048–1065.
7 J.-L. Ravanat, T. Douki and J. Cadet, *J. Photochem. Photobiol., B*, 2001, **63**, 88–102.
8 R. P. Sinha and D.-P. Häder, *Photochem. Photobiol. Sci.*, 2002, **1**, 225–236.
9 M. Koga, M. Asplund and D. M. Neumark, *J. Chem. Phys.*, 2022, **156**, 244302.
10 R. P. Rastogi, Richa, A. Kumar, M. B. Tyagi and R. P. Sinha, *J. Nucleic Acids*, 2010, **2010**, 592980.
11 M. Asplund, M. Koga, Y. J. Wu and D. M. Neumark, *J. Chem. Phys.*, 2024, **160**, 054301.
12 C. Sagan, *J. Theor. Biol.*, 1973, **39**, 195–200.
13 V. G. Stavros and J. R. Verlet, *Annu. Rev. Phys. Chem.*, 2016, **67**, 211–232.
14 H. Kang, B. Jung and S. K. Kim, *J. Chem. Phys.*, 2003, **118**, 6717–6719.
15 S. Ullrich, T. Schultz, M. Z. Zgierski and A. Stolow, *Phys. Chem. Chem. Phys.*, 2004, **6**, 2796–2801.
16 C. Canuel, M. Mons, F. Piuzzi, B. Tardivel, I. Dimicoli and M. Elhanine, *J. Chem. Phys.*, 2005, **122**, 074316.
17 H. Satzger, D. Townsend, M. Z. Zgierski, S. Patchkovskii, S. Ullrich and A. Stolow, *Proc. Natl. Acad. Sci. U. S. A.*, 2006, **103**, 10196–10201.
18 C. Z. Bisgaard, H. Satzger, S. Ullrich and A. Stolow, *ChemPhysChem*, 2009, **10**, 101–110.
19 N. L. Evans and S. Ullrich, *J. Phys. Chem. A*, 2010, **114**, 11225–11230.
20 S. Perun, A. L. Sobolewski and W. Domcke, *J. Am. Chem. Soc.*, 2005, **127**, 6257–6265.
21 S. Perun, A. L. Sobolewski and W. Domcke, *Chem. Phys.*, 2005, **313**, 107–112.
22 L. Serrano-Andrés, M. Merchán and A. C. Borin, *Proc. Natl. Acad. Sci. U. S. A.*, 2006, **103**, 8691–8696.
23 L. Serrano-Andrés, M. Merchán and A. C. Borin, *Chem. – Eur. J.*, 2006, **12**, 6559–6571.
24 M. Barbatti and H. Lischka, *J. Am. Chem. Soc.*, 2008, **130**, 6831–6839.
25 I. Conti, M. Garavelli and G. Orlandi, *J. Am. Chem. Soc.*, 2009, **131**, 16108–16118.
26 M. Barbatti, A. J. A. Aquino, J. J. Szymczak, D. Nachtigallová, P. Hobza and H. Lischka, *Proc. Natl. Acad. Sci. U. S. A.*, 2010, **107**, 21453–21458.

27 M. Barbatti, Z. Lan, R. Crespo-Otero, J. J. Szymczak, H. Lischka and W. Thiel, *J. Chem. Phys.*, 2012, **137**, 22A503.
28 S. Mandal and V. Srinivasan, *J. Phys. Chem. B*, 2022, **126**, 7077–7087.
29 J.-M. L. Pecourt, J. Peon and B. Kohler, *J. Am. Chem. Soc.*, 2001, **123**, 10370–10378.
30 B. Cohen, P. M. Hare and B. Kohler, *J. Am. Chem. Soc.*, 2003, **125**, 13594–13601.
31 W.-M. Kwok, C. Ma and D. L. Phillips, *J. Am. Chem. Soc.*, 2006, **128**, 11894–11905.
32 G. M. Roberts, H. J. Marroux, M. P. Grubb, M. N. Ashfold and A. J. Orr-Ewing, *J. Phys. Chem. A*, 2014, **118**, 11211–11225.
33 J. Peon and A. H. Zewail, *Chem. Phys. Lett.*, 2001, **348**, 255–262.
34 D. Onidas, D. Markovitsi, S. Marguet, A. Sharonov and T. Gustavsson, *J. Phys. Chem. B*, 2002, **106**, 11367–11374.
35 T. Gustavsson, A. Sharonov, D. Onidas and D. Markovitsi, *Chem. Phys. Lett.*, 2002, **356**, 49–54.
36 T. Pancur, N. K. Schwalb, F. Renth and F. Temps, *Chem. Phys.*, 2005, **313**, 199–212.
37 T. Gustavsson, N. Sarkar, I. Vaya, M. C. Jimenez, D. Markovitsi and R. Improta, *Photochem. Photobiol. Sci.*, 2013, **12**, 1375–1386.
38 M. C. Stuhldreier and F. Temps, *Faraday Discuss.*, 2013, **163**, 173–188.
39 T. Gustavsson and D. Markovitsi, *Acc. Chem. Res.*, 2021, **54**, 1226–1235.
40 F. Buchner, H. H. Ritze, J. Lahl and A. Lübcke, *Phys. Chem. Chem. Phys.*, 2013, **15**, 11402–11408.
41 H. L. Williams, B. A. Erickson and D. M. Neumark, *J. Chem. Phys.*, 2018, **148**, 194303.
42 B. Mennucci, A. Toniolo and J. Tomasi, *J. Phys. Chem. A*, 2001, **105**, 4749–4757.
43 S. Yamazaki and S. Kato, *J. Am. Chem. Soc.*, 2007, **129**, 2901–2909.
44 R. Mitric, U. Werner, M. Wohlgemuth, G. Seifert and V. Bonacic-Koutecky, *J. Phys. Chem. A*, 2009, **113**, 12700–12705.
45 Z. Lan, Y. Lu, E. Fabiano and W. Thiel, *ChemPhysChem*, 2011, **12**, 1989–1998.
46 Y. Lu, Z. Lan and W. Thiel, *J. Comput. Chem.*, 2012, **33**, 1225–1235.
47 F. Santoro, R. Improta, T. Fahleson, J. Kauczor, P. Norman and S. Coriani, *J. Phys. Chem. Lett.*, 2014, **5**, 1806–1811.
48 S. K. Khani, R. Faber, F. Santoro, C. Hattig and S. Coriani, *J. Chem. Theory Comput.*, 2019, **15**, 1242–1254.
49 V. Ludwig, Z. M. da Costa, M. S. do Amaral, A. C. Borin, S. Canuto and L. Serrano-Andrés, *Chem. Phys. Lett.*, 2010, **492**, 164–169.
50 M. Dreyfus, G. Dodin, O. Bensaude and J. Dubois, *J. Am. Chem. Soc.*, 1975, **97**, 2369–2376.
51 M. T. Chenon, R. J. Pugmire, D. M. Grant, R. P. Panzica and L. B. Townsend, *J. Am. Chem. Soc.*, 1975, **97**, 4636–4642.
52 H. R. Hudock, B. G. Levine, A. L. Thompson, H. Satzger, D. Townsend, N. Gador, S. Ullrich, A. Stolow and T. J. Martínez, *J. Phys. Chem. A*, 2007, **111**, 8500–8508.
53 M. Barbatti and S. Ullrich, *Phys. Chem. Chem. Phys.*, 2011, **13**, 15492–15500.
54 Y. Miura, Y.-i Yamamoto, S. Karashima, N. Orimo, A. Hara, K. Fukuoka, T. Ishiyama and T. Suzuki, *J. Am. Chem. Soc.*, 2023, **145**, 3369–3381.
55 C. W. West, J. Nishitani, C. Higashimura and T. Suzuki, *Mol. Phys.*, 2021, **119**, e1748240.
56 N. Orimo, Y.-i Yamamoto, S. Karashima, A. Boyer and T. Suzuki, *J. Phys. Chem. Lett.*, 2023, **14**, 2758–2763.
57 S. Karashima, Y.-I. Suzuki, Y.-I. Yamamoto and T. Suzuki, *Bull. Chem. Soc. Jpn.*, 2023, **97**, uoad012.
58 J. Hummert, G. Reitsma, N. Mayer, E. Ikonnikov, M. Eckstein and O. Kornilov, *J. Phys. Chem. Lett.*, 2018, **9**, 6649–6655.
59 C. Arrell, J. Ojeda, L. Mewes, J. Grilj, F. Frassetto, L. Poletto, F. Van Mourik and M. Chergui, *Phys. Rev. Lett.*, 2016, **117**, 143001.
60 J. Ojeda, C. A. Arrell, L. Longetti, M. Chergui and J. Helbing, *Phys. Chem. Chem. Phys.*, 2017, **19**, 17052–17062.
61 C. Wang, M. D. Waters, P. Zhang, J. Suchan, V. Svoboda, T. T. Luu, C. Perry, Z. Yin, P. Slavíček and H. J. Wörner, *Nat. Chem.*, 2022, **14**, 1126–1132.
62 I. Jordan, M. Huppert, D. Rattenbacher, M. Peper, D. Jelovina, C. Perry, A. Von Conta, A. Schild and H. J. Wörner, *Science*, 2020, **369**, 974–979.
63 R. Al-Obaidi, M. Wilke, M. Borgwardt, J. Metje, A. Moguilevski, N. Engel, D. Tolksdorf, A. Raheem, T. Kampen and S. Mähl, *New J. Phys.*, 2015, **17**, 093016.
64 J. D. Koralek, J. B. Kim, P. Brůža, C. B. Curry, Z. Chen, H. A. Bechtel, A. A. Cordones, P. Sperling, S. Toleikis, J. F. Kern, S. P. Moeller, S. H. Glenzer and D. P. DePonte, *Nat. Commun.*, 2018, **9**, 1353.
65 M. H. Elkins, H. L. Williams and D. M. Neumark, *J. Chem. Phys.*, 2015, **142**, 234501.
66 M. H. Elkins, H. L. Williams and D. M. Neumark, *J. Chem. Phys.*, 2016, **144**, 184503.
67 P. Kruit and F. H. Read, *J. Phys. E: Sci. Instrum.*, 1983, **16**, 313–324.
68 N. Preissler, F. Buchner, T. Schultz and A. Lübcke, *J. Phys. Chem. B*, 2013, **117**, 2422–2428.
69 N. Kurahashi, S. Karashima, Y. Tang, T. Horio, B. Abulimiti, Y.-I. Suzuki, Y. Ogi, M. Oura and T. Suzuki, *J. Chem. Phys.*, 2014, **140**, 174506.
70 M. Faubel, B. Steiner and J. P. Toennies, *J. Chem. Phys.*, 1997, **106**, 9013–9031.
71 B. A. Abd-El-Nabey, S. El-Housseiny and M. A. Abd-El-Fatah, *Sci. Rep.*, 2022, **12**, 15346.
72 C. Lee, M. N. Pohl, I. A. Ramphal, W. Yang, B. Winter, B. Abel and D. M. Neumark, *J. Phys. Chem. A*, 2022, **126**, 3373–3383.
73 W. Yang, C. Lee, S. Saric, M. N. Pohl and D. M. Neumark, *J. Chem. Phys.*, 2023, **159**, 054704.
74 D. Stemer, T. Buttersack, H. Haak, S. Malerz, H. C. Schewe, F. Trinter, K. Mudryk, M. Pugini, B. Credidio, R. Seidel, U. Hergenhahn, G. Meijer, S. Thürmer and B. Winter, *J. Chem. Phys.*, 2023, **158**, 234202.

75 Y.-i Yamamoto, H. Yano, S. Karashima, R. Uenishi, N. Orimo, J. Nishitani and T. Suzuki, *Bull. Chem. Soc. Jpn.*, 2023, **96**, 938–942.
76 J. P. Brichta, M. C. H. Wong, J. B. Bertrand, H. C. Bandulet, D. M. Rayner and V. R. Bhardwaj, *Phys. Rev. A: At., Mol., Opt. Phys.*, 2009, **79**, 033404.
77 L. Miaja-Avila, C. Lei, M. Aeschlimann, J. Gland, M. Murnane, H. Kapteyn and G. Saathoff, *Phys. Rev. Lett.*, 2006, **97**, 113604.
78 T. Glover, R. Schoenlein, A. Chin and C. Shank, *Phys. Rev. Lett.*, 1996, **76**, 2468.
79 G. Saathoff, L. Miaja-Avila, M. Aeschlimann, M. M. Murnane and H. C. Kapteyn, *Phys. Rev. A: At., Mol., Opt. Phys.*, 2008, **77**, 022903.
80 I. Velchev, W. Hogervorst and W. Ubachs, *J. Phys. B: At., Mol. Opt. Phys.*, 1999, **32**, L511.
81 R. D. Knight and L.-g Wang, *J. Opt. Soc. Am. B*, 1985, **2**, 1084–1087.
82 B. Winter, R. Weber, W. Widdra, M. Dittmar, M. Faubel and I. Hertel, *J. Phys. Chem. A*, 2004, **108**, 2625–2632.
83 S. Thürmer, S. Malerz, F. Trinter, U. Hergenhahn, C. Lee, D. M. Neumark, G. Meijer, B. Winter and I. Wilkinson, *Chem. Sci.*, 2021, **12**, 10558–10582.
84 W. C. Martin, *J. Phys. Chem. Ref. Data*, 1973, **2**, 257–266.
85 C. A. Schroeder, E. Pluharova, R. Seidel, W. P. Schroeder, M. Faubel, P. Slavicek, B. Winter, P. Jungwirth and S. E. Bradforth, *J. Am. Chem. Soc.*, 2015, **137**, 201–209.
86 Z. N. Heim and D. M. Neumark, *Acc. Chem. Res.*, 2022, **55**, 3652–3662.
87 S. Peng, A. Padva and P. R. LeBreton, *Proc. Natl. Acad. Sci. U. S. A.*, 1976, **73**, 2966–2968.
88 A. B. Trofimov, J. Schirmer, V. B. Kobychev, A. W. Potts, D. M. P. Holland and L. Karlsson, *J. Phys. B: At., Mol. Opt. Phys.*, 2005, **39**, 305–329.
89 C. Su, C. T. Middleton and B. Kohler, *J. Phys. Chem. B*, 2012, **116**, 10266–10274.
90 J. M. L. Pecourt, J. Peon and B. Kohler, *J. Am. Chem. Soc.*, 2001, **123**, 10370–10378.
91 M. K. Kuimova, J. Dyer, M. W. George, D. C. Grills, J. M. Kelly, P. Matousek, A. W. Parker, X. Z. Sun, M. Towrie and A. M. Whelan, *Chem. Commun.*, 2005, 1182–1184.
92 G. W. Doorley, M. Wojdyla, G. W. Watson, M. Towrie, A. W. Parker, J. M. Kelly and S. J. Quinn, *J. Phys. Chem. Lett.*, 2013, **4**, 2739–2744.
93 N. Ikeda, N. Nakashima and K. Yoshihara, *J. Phys. Chem.*, 1984, **88**, 5803–5806.
94 H. Miyasaka, M. Hagihara, T. Okada and N. Mataga, *Chem. Phys. Lett.*, 1992, **188**, 259–264.
95 H. Xu and S. Pratt, *J. Phys. Chem. A*, 2013, **117**, 9331–9342.
96 N. J. Kim, G. Jeong, Y. S. Kim, J. Sung, S. Keun Kim and Y. D. Park, *J. Chem. Phys.*, 2000, **113**, 10051–10055.
97 Y. Lee, M. Schmitt, K. Kleinermanns and B. Kim, *J. Phys. Chem. A*, 2006, **110**, 11819–11823.
98 C. Plützer and K. Kleinermanns, *Phys. Chem. Chem. Phys.*, 2002, **4**, 4877–4882.
99 A. Broo, *J. Phys. Chem. A*, 1998, **102**, 526–531.
100 R. W. Wilson and P. R. Callis, *Photochem. Photobiol.*, 1980, **31**, 323–327.
101 C. M. Marian, M. Kleinschmidt and J. Tatchen, *Chem. Phys.*, 2008, **347**, 346–359.
102 Y.-i Yamamoto and T. Suzuki, *J. Phys. Chem. Lett.*, 2020, **11**, 5510–5516.